INORGANIC CHEMISTRY FRONTIERS

RESEARCH ARTICLE

View Article Online
View Journal

Cite this: DOI: 10.1039/d5qi01203a

Tuning multifunctional stimuli-responsive behaviour through halogen exchange in hybrid ionic $[(CH_3CH_2)_3N(CH_2X)]_2[MnCl_4]$ (X = Cl, Br)†

Javier García-Ben, [a] María Gelpi, [a] Pedro Dafonte-Rodríguez, [a] Ángel Ferradanes-Martínez, [a] Ignacio Delgado-Ferreiro,[a] Jorge López-Beceiro,[b] Ramón Artiaga,[b] Antonio Luis Llamas-Saiz, [c] Julian Walker, [d] Charles James McMonagle,[e] Alberto García-Fernández, [a,f] Ute B. Cappel, [f,g] Socorro Castro-García, [a] María Antonia Señarís-Rodríguez, [a] Juan Manuel Bermúdez-García *[a] and Manuel Sánchez-Andújar *[a]

Received 28th May 2025,
Accepted 14th July 2025

DOI: 10.1039/d5qi01203a

rsc.li/frontiers-inorganic

Hybrid metal halide materials have attracted significant attention due to their diverse functional properties. In this study, we prepared, characterized, and evaluated the multifunctional properties of two hybrid tetrachloromanganate(II) compounds with the general formula $[(CH_3CH_2)_3N(CH_2X)]_2[MnCl_4]$, where X is Cl or Br. From the structural point of view, these compounds consist of two isolated ionic species with an antifluorite crystal arrangement: 0D tetrahedral $[MnCl_4]^{2-}$ anions and large, quasi-spherical and polar $[(CH_3CH_2)_3N(CH_2X)]^+$ cations. These cations are responsible for the first-order phase transition observed at $T_t \sim 318$ K for the Cl-compound and $T_t \sim 343$ K for the Br-compound. We investigated various functional properties—specifically dielectric, photoluminescent, and pressure responses—and our results demonstrate that these compounds are highly versatile, exhibiting broad responses to external stimuli. Furthermore, we found that substituting the halogen in the ammonium cations from Cl to Br induces important modifications in their functional properties. In particular, this halogen exchange increases the phase transition temperature, reduces the thermal hysteresis, improves the photoluminescence quantum yield, and enhances the reversible entropy changes under compression–decompression cycles.

1. Introduction

Multifunctional stimuli-responsive materials represent an emerging class of advanced materials that exhibit adaptive responses to a wide range of chemical and physical stimuli.[1] These materials can respond to variations in temperature, pH, light, electric or magnetic fields, pressure, and other factors, leading to changes in thermal, optical, electrical, magnetic, mechanical properties, as well as guest molecule adsorption.[2–7] Consequently, these materials are increasingly in demand for applications in nanotechnology, biomedicine, optoelectronics, and smart material engineering, opening new possibilities for the fabrication of adaptive and highly efficient devices.[1,8]

In recent years, hybrid metal halide compounds, which integrate organic cations with metal halide anions, have garnered significant attention in scientific community.[3,9–20] These materials showcase a diverse array of functional properties, including ferroelectric,[10,20] magnetic,[15] optoelectronic[17–19] and barocaloric.[11,14] Their properties can be finely tuned by modifying the organic and inorganic components. Furthermore, the structural motifs of these compounds vary widely, ranging from highly extended structures to lower dimensional ones, contingent upon the combinations of metal halide anions and organic cations.

Mn^{2+}-based halide hybrids in particular, have garnered attention for light-emission related applications due to their

[a]CICA - Centro Interdisciplinar de Química e Bioloxía, Departamento de Química, Facultade de Ciencias, Universidade da Coruña. Campus de Elviña e Zapateira 15071 A Coruña, Spain. E-mail: j.bermudez@udc.es, m.andujar@udc.es
[b]CITENI-Proterm Group, Ferrol Industrial Campus, Campus de Esteiro, University of A Coruna, Ferrol, 15403 Spain
[c]Research Infrastructures Area, X-ray Unit, University of Santiago de Compostela, 15782 Santiago de Compostela, Spain
[d]Norwegian University of Science and Technology, Department of Materials Science and Engineering, Trondheim 7491, Norway
[e]European Synchrotron Radiation Facility, Swiss-Norwegian Beamlines, Grenoble 3843, France
[f]Division of X-ray Photon Science, Department of Physics and Astronomy, Uppsala University, Box 516, SE-751 20 Uppsala, Sweden
[g]Wallenberg Initiative Materials Science for Sustainability, Department of Physics and Astronomy, Uppsala University, 751 20 Uppsala, Sweden

†Electronic supplementary information (ESI) available. CCDC 2427806–2427812. For ESI and crystallographic data in CIF or other electronic format see DOI: https://doi.org/10.1039/d5qi01203a

advantages, tuneable luminescence, stability, nonlinear optical effects and high photoluminescence quantum yield (PLQY).[21,22] It is well known that the emission colour of Mn^{2+} is significantly influenced by the metal's coordination environment.[23,24] Specifically, when Mn^{2+} is coordinated in an octahedral arrangement, the emission colour is red. In contrast, zero-dimensional (0D) hybrid Mn^{2+} halides containing isolated tetrahedral anions MnX_4^{2-} (X = Cl, Br) exhibit green emission, which is characterized by a large Stokes shift and a high PLQY that can reach up to 90%.[25]

In previous studies, we have designed and studied hybrid organic-ionic plastic crystals for multi-energy storage, specifically solar thermal energy storage and electric,[3,9,16] as well as for multipurpose pressure-induced barocaloric refrigeration and passive cold-storage.[26–28]

Now, we extend these studies trying to identify new hybrid plastic crystals with multifunctional stimuli-responsiveness for different technological applications, including solid-state refrigeration induced by pressure and UV-activated photoluminescence modulated by temperature. We also aim to modify those properties and stimuli-response by simple chemical modifications.

For that purpose, we focus on two analogue compounds formed by tetrachloromanganate(II) anions –$[MnCl_4]^{2-}$– combined with polar cations of large-size and quasi-spherical, specifically the $[(CH_3CH_2)_3N(CH_2X)]^+$ (X = Cl, Br) cations. These spherical cations feature a rigid inner core and a flexible outer shell with a significant degree of rotational freedom due to the rotatable C–N and C–C bonds.[29] The polar nature and structural flexibility of these cations make them particularly suited for designing multiresponsive materials that can react to electric fields, temperature and external pressure.

We have synthesised these compounds, were the Cl-analogue is already described[30] while the Br-analogue is novel, and characterized their crystal structure by variable temperature single crystal X-ray diffraction and variable temperature synchrotron powder X-ray diffraction. Additionally, we have investigated their response towards different external stimuli, including temperature, light, alternating electric fields and pressure. The observed responses reinforce the versatility of 0D hybrid tetrahalidemanganate(II) compounds as chemically-tuneable multifunctional and stimuli-responsive materials.

2. Experimental section

2.1. Synthesis

Commercially available reagent grade manganese(II) chloride tetrahydrate (≥97% Sigma-Aldrich), triethylamine (99% Sigma-Aldrich), dichloromethane (≥99.9% Sigma-Aldrich), dibromomethane (99% Sigma-Aldrich) and hydrochloric acid (37% Thermo Scientific) were used as starting materials without further purification.

As we previously described,[31] the compounds $[(CH_3CH_2)_3N(CH_2X)]X$ with X = Cl, Br were prepared by mixing triethylamine with an excess of CH_2X_2 and stirring at room temperature for 72 hours. The resulting white solids were obtained by removing the solvent under reduced pressure at 343 K, and the formation of $[(CH_3CH_2)_3N(CH_2Cl)]Cl$ and $[(CH_3CH_2)_3N(CH_2Br)]Br$ was corroborated by NMR spectroscopy.

In the next step, $[(CH_3CH_2)_3N(CH_2Br)]Cl$ was prepared by anion exchange of the previously obtained $[(CH_3CH_2)_3N(CH_2Br)]Br$. For this purpose, an Amberlite IRA-400 chloride form ion-exchange resin was used. The $[(CH_3CH_2)_3N(CH_2Br)]Br$ compound was passed through the resin three times. To ensure the complete replacement of Br^- anions by Cl^-, $AgNO_3$ was added to a solution of $[(CH_3CH_2)_3N(CH_2Br)]Cl$, resulting in the precipitation of AgCl. The precipitate was analyzed by micro X-ray fluorescence (μ-XRF) to confirm the absence of Br^- anions, see Fig. S1 of ESI.† As is well established, the presence of Br^- anions in the coordination environment of Mn^{2+} cations can significantly affect photoluminescence properties.[23,24]

Finally, aqueous solutions (5 mL) of $[(CH_3CH_2)_3N(CH_2Cl)]Cl$ (2.90 mmol, 0.80 g) and $[(CH_3CH_2)_3N(CH_2Br)]Cl$ (2.90 mmol, 0.67 g) were prepared and mixed with an aqueous solution (5 mL) of $MnCl_2{\cdot}4H_2O$ (1.45 mmol, 0.29 g), and 1 mL of HCl was added to the mixture at room temperature. After one week, small colourless crystals were obtained and dried in a vacuum desiccator (yield: ~65%).

2.2. Single crystal X-ray diffraction (SCXRD)

Single-crystal X-ray diffraction (SCXRD) experiments were carried out at 100, 150, 200, 250, 293, 313 and 333 K. For that purpose, single-crystal diffraction data sets of two crystals taken from the same batch of the Cl-compound were collected in a Bruker D8 VENTURE Kappa X-ray diffractometer equipped with a PHOTON III detector and using monochromatic MoKα radiation (λ = 0.71073 Å).

The crystals were mounted on MiTeGen MicroMountTM using Paratone® N (Hampton Research). The data integration and reduction were performed using the APEX4 v2021.10-0 (Bruker AXS, 2021) software suite. The integrations of the reflections were performed with SAINT 8.40B and the intensities collected were corrected for Lorentz and polarization effects and for absorption by semi-empirical methods on the basis of symmetry-equivalent data using SADABS 2016/2 of the suite software. The structures were solved by the dual-space algorithm implemented in SHELXT2014/5 program[32] and were refined by least squares method on SHELXL2018/3. (Table S1†).

2.3. Powder X-ray diffraction (PXRD) and synchrotron powder X-ray diffraction (SPXRD)

Powder X-ray diffraction (PXRD) patterns of the obtained polycrystalline powders were collected in a Siemens D-5000 diffractometer using CuKα radiation at room temperature.

Synchrotron powder X-ray diffraction (SPXRD) pattern of $[(CH_3CH_2)_3N(CH_2X)][MnCl_4]$ (X = Cl, Br) were collected on Swiss-Norwegian beamline BM01 beamline at ESRF (Grenoble, France) using a wavelength of 0.601 Å. Patterns were collected as a function of temperature from 200 to 400 K using a Cryostream to control the temperature. The wavelength was determined using PyFai software[33] by refining the positions of

all available reflections of LaB_6 collected with a Pilatus 2 M detector at a sample-to-detector distance of 163 mm. The recorded 2D images were azimuthally integrated into a 1D powder profile using Bubble.[34] The sample was loaded into a thin-walled borosilicate glass capillary, 0.5 mm diameter, and rotated during the exposer for better powder averaging. Le Bail analysis were carried out using the program GSAS-II.[35]

Additionally, we have calculated the volumetric coefficients of the thermal expansion (TE) from the obtained lattice parameters, using the web-based tool PASCal version v2.2.0 (principal axis strain calculator; https://www.pascalapp.co.uk/).[36]

2.4. Thermal analysis

Thermogravimetric analyses (TGA) were carried out in a TGA-DTA Thermal Analysis SDT2960 equipment. Approximately 18 mg of powder were heated at a rate of 10 K min^{-1} from 300 K to 1270 K for the experiment, using a alumina crucible, under a flow of dry nitrogen.

Differential scanning calorimetric (DSC) analysis were carried out in a TA Instruments MDSC Q2000 by heating and cooling the samples under a nitrogen atmosphere, during several cycles at 10 K min^{-1} from 293 K up to 520 K.

Variable pressure differential scanning calorimetry (VP-DSC) was performed using a Setaram μDSC7 EVO microcalorimeter equipped with a Syrixus 65x Isco pressure pump. Samples of mass ~20 mg were tested at various isobaric conditions from 1 to 1000 bar in the temperature range of 290–380 K, using a 1.2 K min^{-1} heating/cooling rate and at various isotherm conditions from 345 to 351 K, in the pressure range of 100–1000 bar, using a 10 bar min^{-1} compression/decompression rate.

2.5. Photoluminescence spectroscopy

Emission and excitation spectra were measured on a Horiba FluoroMax Plus-P spectrofluorometer equipped with a 150 W ozone-free xenon arc lamp and a R928P photon-counting emission detector, as well as a photodiode reference detector for monitoring lamp output. Samples were excited using a 150 W Xenon arc lamp at 360 nm for photoluminescence emission spectra while at 518 nm for photoluminescence excitation spectra.

Time-resolved photoluminescence decays were measured on a Horiba FluoroMax Plus-P spectrofluorometer working in the phosphorescence lifetime Spectroscopy mode, using 360 nm as an excitation wavelength.

Temperature-dependent luminescence measurements were performed with a cryo-stage, Linkam THMS-LNP95 cooling/heating system.

The absolute quantum yield (QY) was measured with a G8 integrating sphere (GMP), using $BaSO_4$ as blank at 298 K.

2.6. Dielectric properties

The complex dielectric permittivity ($\varepsilon_r = \varepsilon'_r - i\varepsilon''_r$) of cold-press pelletized samples was measured as a function of frequency and temperature with a parallel-plate capacitor coupled to a Solartron1260A Impedance/Gain-Phase Analyzer, capable to measure in the frequency range from 1 Hz up to 1 MHz using an amplitude of 1 V. The capacitor was mounted in a Janis SVT200T cryostat refrigerated with liquid nitrogen and with a Lakeshore 332 incorporated to control the temperature from 100 K up to 400 K. The data were collected on heating, and before carrying out the measurement the pellets were maintained at each temperature for 2 minutes, so as to allow them to reach thermal equilibrium. Pelletized samples, with an area of approximately 133 mm^2 and a thickness of approximately 1 mm, were prepared by cold-press to fit into the capacitor. Gold was previously sputtered on the surfaces of the pelletized samples to ensure a good electrical contact. All the dielectric measurements were carried out in a nitrogen atmosphere, performing several cycles of vacuum and nitrogen gas to ensure a sample environment free of water.

2.7. Micro X-ray fluorescence spectrometry (μ-XRF)

Micro X-ray fluorescence spectrometry (μ-XRF) was performed directly, under vacuum, in a M4 Tornado microfluorescence spectrometer (Bruker-AXS), equipped with a 30 W Rh tube with polycapillary optics and a double solid-state detector (XFlash).

3. Results and discussion

3.1. Basic characterization

The two $[(CH_3CH_2)_3N(CH_2X)]_2[MnCl_4]$ (X = Cl, Br) compounds were obtained as polycrystalline powder by grinding the single crystals. The purity was confirmed by comparison of the experimental PXRD patterns with those simulated patterns from single crystal structures at 293 K (Fig. S2 of ESI†).

According to the TGA results (Fig. S3 of ESI†), these $[(CH_3CH_2)_3N(CH_2X)]_2[MnCl_4]$ compounds are stable up to $T \sim$ 495 K (when X = Cl) and $T \sim$ 465 K (when X = Br).

Variable-temperature differential scanning calorimetry (VT-DSC) experiments at ambient pressure revealed that both compounds experience a reversible phase transition slightly above room temperature (Fig. 1) occurring at $T_t \sim$ 318 K (X = Cl) and ~343 K (X = Br) on heating and at $T_t \sim$ 305 K (X = Cl) and ~338 K (X = Br) on cooling.

The observed hysteresis indicates the first-order character of such phase transition, that in the case of X = Cl involves an enthalpy change of $\Delta H \sim$ 19 kJ kg^{-1} and an entropy change of $\Delta S \sim$ 60 J K^{-1} kg^{-1}, as determined from the area under the C_p/T curve and the peak temperature, $T_{max.}$. Meanwhile, when X = Br the observed thermal changes are around 30% lower (see Table 1).

Taking into account that for an order–disorder transition $\Delta S = R\ln(N)$, where R is the gas constant and N is the ratio of the number of configurations in the disordered and ordered system, we obtain values of $N \sim$ 32 (X = Cl) and ~14 (X = Br). The obtained results suggest a more severe disorder in the Cl-compound than in the Br-compound.

In turn, the obtained values for $[(CH_3CH_2)_3N(CH_2Cl)]_2[MnCl_4]$ are similar to those reported in the literature.[30]

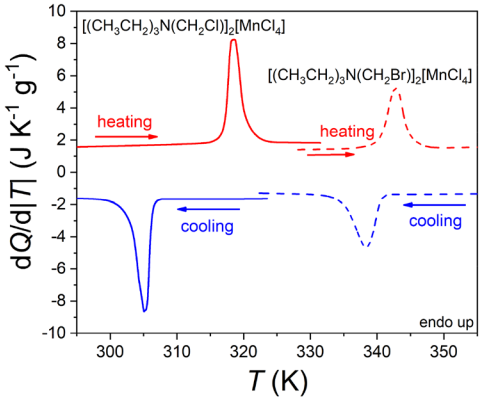

Fig. 1 VT-DSC curves at ambient pressures for $[(CH_3CH_2)_3N(CH_2Cl)]_2[MnCl_4]$ (solid lines) and $[(CH_3CH_2)_3N(CH_2Br)]_2[MnCl_4]$ (dash lines) from 295 to 355 K.

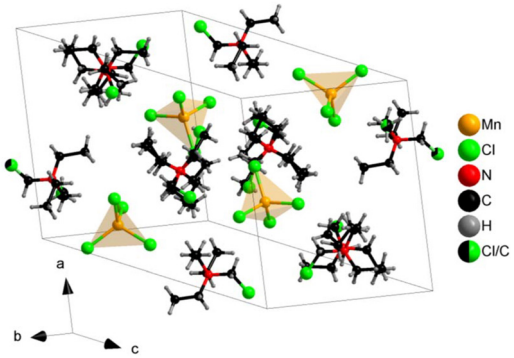

Fig. 2 Crystal structure of the LT-phase for $[(CH_3CH_2)_3N(CH_2Cl)]_2[MnCl_4]$ compound obtained by SCXRD.

Table 1 Thermodynamic parameters of the observed phase transitions from DSC data for $[(CH_3CH_2)_3N(CH_2Cl)]_2[MnCl_4]$ and $[(CH_3CH_2)_3N(CH_2Br)]_2[MnCl_4]$ compounds

Compound	T_t (K)	ΔH (kJ kg^{-1})	ΔS (J K^{-1} kg^{-1})
$[(CH_3CH_2)_3N(CH_2Cl)]_2[MnCl_4]$	318 (h)	18 (h)	58 (h)
	305 (c)	19 (c)	62 (c)
$[(CH_3CH_2)_3N(CH_2Br)]_2[MnCl_4]$	343 (h)	13 (h)	38 (h)
	338 (c)	13 (c)	39 (c)

(h) = heating and (c) = cooling.

3.2. Crystal structures of $[(CH_3CH_2)_3N(CH_2Cl)]_2[MnCl_4]$ by variable temperature single-crystal X-ray diffraction

Single-crystal X-ray diffraction experiments in $[(CH_3CH_2)_3N(CH_2Cl)]_2[MnCl_4]$ were carried out at different temperatures (100, 150, 200, 250, 293, 313 and 333 K), well above and below the observed DSC transition to determine the evolution of the crystal structure.

As for the low temperature polymorph (LT) present at $T < T_t$ it shows triclinic symmetry with space group $P\bar{1}$ in the temperature range of 100–293 K (see more details on Fig. 2 and Table S1 of ESI†). These results are in line with the already described structure. In the following paragraphs we will add new discussions and observations of the crystal structure of the LT-phase that are relevant to understand the properties and comparison described in this work.

The asymmetric unit contains two different crystallographic $[MnCl_4]^{2-}$ anions and four different $[(CH_3CH_2)_3N(CH_2Cl)]^+$ cations. The two $[MnCl_4]^{2-}$ tetrahedra are fully irregular with four different Mn–Cl bond lengths and Cl–Mn–Cl angles slightly different from the ideal angle 109.5° (see details on Tables S2 and S3 of ESI†) and they are ordered.

In the case of the $[(CH_3CH_2)_3N(CH_2Cl)]^+$ cations they are seen in three different conformations: (i) fully ordered, (ii) partially disordered, showing positional disorder at the Cl atom and the terminal C atoms of one ethyl group, while the other two ethyl groups remain ordered and (iii) fully orientational disordered, with the coexistence of two different orientational cations (see details Fig. S4 of ESI†). While in the temperature range 100–250 one cation (out of the 4) is ordered, two show positional disorder at Cl and one C atoms, and the fourth is orientationally disorder. As temperature increases further ($T >$ 250 K) one of the initially positionally disordered cation changes into a second orientationally disorder situation (see Fig. S4 of ESI†).

We have also analysed the packing of the ionic species in the obtained crystal structure and can show that the molecules form face centre cubic (FCC) close packed anti-fluorite structure. Where, characteristically, the $[MnCl_4]^{2-}$ anions sit in the close packed lattice sites exhibiting a twelve-fold coordination, with six other $[MnCl_4]^{2-}$ tetrahedra on the same plane and another three above and below the plane. The molecular cations fill all four of the tetrahedral sites in the FCC structure as is characteristic of an anti-fluorite structure (see Fig. S5 of ESI†). Where the locations of the anions and cations are reversed relative to fluorite structure.

Moreover, we have studied the intermolecular interactions between cations and anions using the Hirshfeld surface implemented on the CrystalExplorer software.[37] From the analysis of the fingerprint plot, we find close contacts occurring between the Cl-atoms of the $[MnCl_4]^{2-}$ anion and the H-atoms of the cations (see Fig. S6 of ESI†). In this context, the shortest distance found between $[MnCl_4]^{2-}$ anion and the H-atoms of the chloride methyl group is 3.53 Å at 100 K (see Fig. S7 of ESI†). Such H-atoms that are close to a strongly electronegative Cl, which causes a weakening of the C–H bond and separation of charge, though an inductive effect favouring the observed intermolecular interaction. On this turn, the Cl-atom of the $[MnCl_4]^{2-}$ anion, involved in this intermolecular contact, shows the longest Mn–Cl bond length (2.39 Å), reflecting the concomitant weakening of this intramolecular bond. Additionally, we observe that the $[(CH_3CH_2)_3N(CH_2Cl)]^+$ cations involved in these interactions are fully ordered, revealing the relevance of such intermolecular interactions in the conformation of the cation.

The HT-phase (high temperature polymorph) shows tetragonal symmetry with space group $P4_2/nmc$ (no: 137) (see more details on Fig. 3 and Table S1 of ESI†).

The crystal structure of HT-phase has a similar packing to that of LT-phase, even if the $[MnCl_4]^{2-}$ tetrahedral is almost regular at the HT-phase, where all Mn–Cl bond lengths are identical, and the Cl–Mn–Cl angles are very close to the ideal angle 109.5° (see details on Table S2 of ESI†). Also, all the $[(CH_3CH_2)_3N(CH_2Cl)]^+$ cations exhibit an orientational disorder at the HT-phase.

In summary, the phase transition observed near 313 K in the $[(CH_3CH_2)_3N(CH_2Cl)]_2[MnCl_4]$ compound is primarily driven by changes in the behavior of the $[(CH_3CH_2)_3N(CH_2Cl)]^+$ cations, while the $[MnCl_4]^{2-}$ anions remain fully ordered in both phases.

In the LT-phase the cations are in three states: completely ordered, positionally disordered or orientationally disordered (see Fig. S4 of ESI†). In the partially disordered state, the cations remain static—that is, they do not change their conformations—as the temperature approaches the transition point from below. As the temperature nears 313 K, the cations gradually gain enough energy to begin dynamic reorientations, marking the onset of increased disorder. Beyond 313 K, the compound undergoes a polymorphic transformation. In this new phase, all the cations exhibit dynamic orientational disorder and are rapidly reoriented. This interplay between the static-to-dynamic changes and the order–disorder transition of the cations is the key factor underlying the overall phase change in this compound.

3.3. Variable-temperature synchrotron powder X-ray diffraction (SPXRD)

The Br-compound was analysed using variable-temperature synchrotron powder X-ray diffraction (SPXRD). This was performed in part due to the inability to grow sufficiently large single crystals for analysis. To adequately characterize the phase transition, variable temperature SPXRD patterns were collected within the temperature range of 200–400 K. As shown in Fig. 4, a clear phase transition is seen to occur at $T \sim 335$ K, in agreement with DSC results.

Le Bail refinements of the obtained patterns indicate that the room temperature phase (LT-phase) shows triclinic with a space group $P\bar{1}$ and lattice parameters at T = 200 K: a = 13.373(1) Å, b = 13.821(1) Å, c = 16.220(2) Å, α = 110.214(2)°, β = 112.679(2)°, γ = 91.456(1) (see Fig. S8 of ESI†). It is worth to note that the obtained lattice parameters are very similar to those obtained for the Cl-compound, even if slightly higher d, which seems to be related with the larger size of the Br-atoms. This finding suggests that both Br- and Cl-compounds are isostructural in the LT-phase.

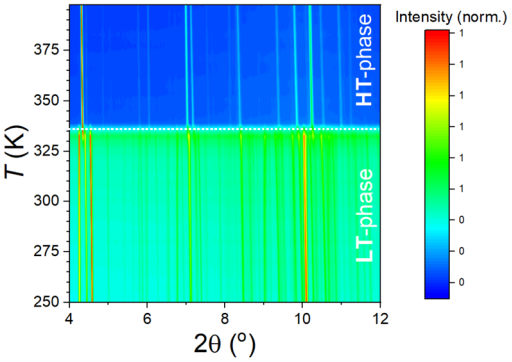

Fig. 4 SPXRD patterns of $[(CH_3CH_2)_3N(CH_2Br)]_2[MnCl_4]$ as a function of temperature (250 K < T < 395 K).

On the other hand, the HT-phase was successfully fitted (see Fig. S9 of ESI†) to a tetragonal symmetry with a space group $I4_1/a$ (no: 88) and lattice parameters at T = 343 K, a = 13.7055 (1) Å and c = 28.4615 (4) Å a crystal structure with lower symmetry $P4_2/nmc$ (no: 137) than that of the related Cl-compound even if it resembles a superstructure of the former, since $a_{Br} \sim \sqrt{2}a_{Cl}$ and $c_{Br} \sim 2a_{Cl}$. Therefore, in view of the significant differences observed in the crystal structure and latent heat associated with the phase transition of both compounds we suggest that the high-temperature (HT) phase of the Br-compound exhibits lower degree of disorder compared to that of the Cl-compound.

Fig. 5 shows the thermal evolution of the lattice volume per formula of the Br-compound, which has been obtained from Le Bail fitting of the SXRPD patterns at different temperatures.

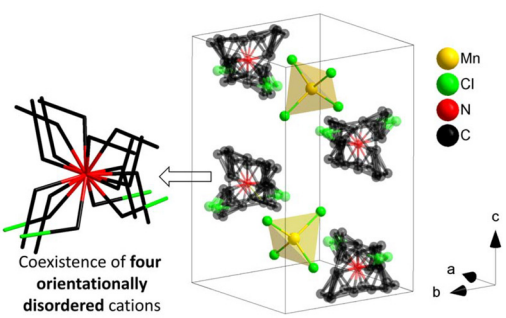

Fig. 3 Crystal structure of the HT-phase for $[(CH_3CH_2)_3N(CH_2Cl)]_2[MnCl_4]$ compound obtained by SCXRD.

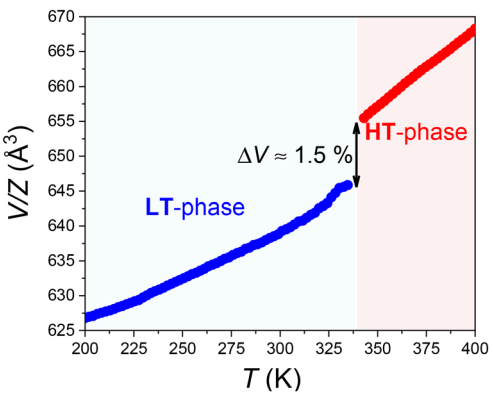

Fig. 5 Evolution of the volume cell of both phases of $[(CH_3CH_2)_3N(CH_2Br)]_2[MnCl_4]$ as a function of temperature.

It can be seen there a rather abrupt volume change occurs at $T_t \sim 340$ K, which is associated to a phase transition. As for the volumetric TE coefficients obtained for the LT and HT phase: $2.17(2) \times 10^{-4}$ K^{-1} and $3.35(2) \times 10^{-4}$ K^{-1} respectively, their values are similar to those reported for analogues compounds, such as $[choline]_2CoCl_4$ with TE coefficient of 2.17(8) 10^{-4} K^{-1}.[38]

As for the volume change occurring at T_t ($\Delta V = 1.5\%$), see Fig. 5, it is in the range of similar reported molecular compounds, even if it is lower than the case of $[(CH_3)_3NOH]_2CoCl_4$ ($\Delta V = 2.6\%$ at $T \sim 343$ K),[28] quinuclidinium perrhenate, $[C_7H_{14}N][ReO_4]$ ($\Delta V = 2.7\%$ at $T \sim 340$ K)[14] and tetramethylammonium tetrachloroferrate, $[(CH_3)_4N][FeCl_4]$ ($\Delta V = 3.1\%$ at $T \sim 380$ K),[14] but higher than the diquinuclidinium tetrachloromanganate, $((C_7H_{14}N)_2MnCl_4$ ($\Delta V = 0.4\%$ at 289 K)[39] or the diquinuclidinium tetrachlorocobaltate $[(C_7H_{14}N)_2][CoCl_4]$, $\Delta V = 0.7\%$ at 322 K).[13]

Such volume change can be used to indirectly estimate the barocaloric coefficients (response of the transition temperature towards pressure) associated to the phase transitions following the Clausius–Clapeyron equation (eqn (1)):[40]

$$dT/dp = \Delta V/\Delta S \quad (1)$$

where dT/dp is the pressure dependence of the transition temperature (also known as barocaloric coefficient), ΔV is the volume change in the unit cell and ΔS is the entropy change associated with the phase transition at ambient pressure. By using this method, we estimated that the barocaloric coefficients for the Br- and Cl-compounds are $dT/dp \sim 26$ K kbar^{-1} and $dT/dp \sim 22$ K kbar^{-1}, respectively. These values are discussed in more detail in the next section.

3.4. Pressure-responsiveness and barocaloric properties

In order to understand the response of these materials towards different external stimuli, we first studied the response of the phase transitions to applied pressure. For this purpose, we performed variable-temperature DSC (VT-DSC) studies under different isobaric conditions, as well as variable-pressure DSC (VP-DSC) studies under different isothermal conditions.

In this context, Fig. 6 presents the VT-DSC analysis at different constant pressures (isobaric conditions), ranging from 1 to 1000 bar.

These experiments show that the transition temperature in both compounds shifts towards higher temperatures when increasing the pressure. Interestingly, the transition of the Cl-compound seems to occur in two consecutive steps for pressures above 700 bar, while the Br-compounds exhibit a single step transition in the whole range of pressures.

Nevertheless, the enthalpy change remains almost constant with values of $\Delta H \sim 18$ J g^{-1} and $\Delta H \sim 13$ J g^{-1} for the Cl- and Br-compounds, respectively. This is in fully agreement with the values observed by our VT-DSC studies at ambient temperature.

As it can be observed in the p–T phase diagrams of both compounds (Fig. 7), the transition temperatures are very sensitive towards pressure, with barocaloric (BC) coefficients of up-to $dT_t/dp \sim 19$ K kbar^{-1} upon heating in both cases, similar to the values estimated by the Clausius–Clapeyron equation.

As we show in Fig. 7, the response to applied pressure differs between the two compounds. For the Cl compound, the phase transition temperature shows an anomalous dependence on pressure during the heating and cooling cycles. Specifically, the phase transition temperature increases with pressure with a slope of approximately $dT_t/dp \sim 19$ K kbar^{-1} during heating, and with a lower slope of $dT_t/dp \sim 9$ K kbar^{-1} during cooling. This difference in slopes results in an increase in thermal hysteresis with applied pressure, preventing the Cl-compound from achieving a reversible phase transition under isothermal compression–decompression cycles at pressure below 800 bar. Moreover, the endothermic peaks appearing during heating at pressures below 600 bar display a shoulder, suggesting the presence of two closely phase transitions—a feature that is absent in the corresponding exothermic peaks during cooling. Although the micro-structural origin of this behaviour remains unclear, similar responses have been reported in related hybrid metal halide materials.[11] Notably, the pressure responsiveness values for the Cl compound are comparable to those observed in other reported barocaloric hybrid materials.[14,26,41]

In contrast, the Br compound exhibits unique single-phase transition during both heating and cooling over the entire range of pressures studied, the transition temperature of which increases linearly with pressure. Furthermore, the combination of a relatively small thermal hysteresis and a high barocaloric coefficient promotes full reversibility of the phase

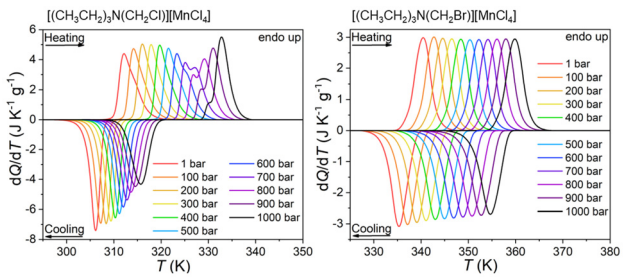

Fig. 6 VT-DSC curves of $[(CH_3CH_2)_3N(CH_2Cl)]_2[MnCl_4]$ (left) and $[(CH_3CH_2)_3N(CH_2Br)]_2[MnCl_4]$ (right) under isobaric conditions from 1 bar to 1000 bar.

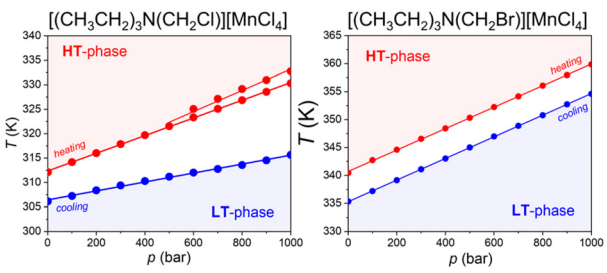

Fig. 7 pvT phase diagram of $[(CH_3CH_2)_3N(CH_2Cl)]_2[MnCl_4]$ (left) and $[(CH_3CH_2)_3N(CH_2Br)]_2[MnCl_4]$ (right) from 1 bar to 1000 bar.

transition under isothermal compression–decompression cycles and across a relatively broad temperature range. These features are essential for the practical application of barocaloric materials.

Additionally, we have analysed the pressure-induced barocaloric properties in terms of reversible isothermal entropy changes (ΔS_{rev}) by using the reported quasi-direct methods[26] following eqn (2):

$$\Delta S_{rev} = \Delta S_{ib}(p \neq 1, T) - \Delta S_{ib}(p = 1, T) \quad (2)$$

where ΔS_{ib} is the isobaric entropy change previously calculated after integrating the curves obtained in Fig. 6.

Fig. 8 shows that a completely reversible phase transition under isothermal compression–decompression cycles is achievable for the Br compound, but not for the Cl compound, consistent with the trends anticipated from the *pvT* phase diagrams (Fig. 7). For $[(CH_3CH_2)_3N(CH_2Cl)]_2[MnCl_4]$, the maximum reversible entropy change $\Delta S_{rev(q-d)}$ is approximately 28 J K^{-1} kg^{-1} under 1000 bar, which is about half of the entropy change (ΔS = 60 J K^{-1} kg^{-1}) observed for the first-order transition at ambient pressure. In contrast, $[(CH_3CH_2)_3N(CH_2Br)]_2[MnCl_4]$ exhibit a $\Delta S_{rev(q-d)}$ of around 35 J K^{-1} kg^{-1} when applying 600 bar, a similar value to the entropy changes at ambient pressure. Moreover, this entropy change can be maintained over a temperature span of about 10 K at 1000 bar, indicating a relatively broad operational range.

In addition, the caloric effects of the Br compound were confirmed *via* direct measurement methods, as reported in the literature,[26] by tuning the pressure from 100 to 1000 bar under various isothermal conditions (see Fig. 9 left).

Fig. 9 shows that a reversible phase transition can be induced isothermally under compression–decompression cycles, with an entropy change of $\Delta S_{rev(q-d)} \sim 38$ J K^{-1} kg^{-1} over an operating temperature range from 345 K to 351 K, which is in agreement with the values observed by quasi-direct analysis. The pressure-induced phase transition exhibits broad peaks and relatively low-pressure hysteresis during the compression–decompression cycles. Additionally, we compared the phase transition temperatures and pressures obtained under isothermal conditions with those measured *via* isobaric conditions (see Fig. 9, right). The results are in good agreement,

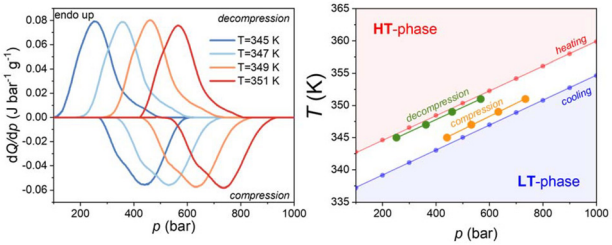

Fig. 9 (Left) VP-DSC curves of $[(CH_3CH_2)_3N(CH_2Br)]_2[MnCl_4]$ under isotherm conditions from 345 to 351 K. (Right) *pvT* phase diagram of $[(CH_3CH_2)_3N(CH_2Br)]_2[MnCl_4]$ comparing data obtained from isothermal and isobaric DSC measurements.

with the barocaloric coefficient $dT_t/dp \approx 19$ K kbar^{-1}, obtaining similar values for both measurements.

In turn, these materials exhibit barocaloric effects and coefficient comparable to most of the best barocaloric hybrid materials and/or plastic crystals,[11,19,24–26,39–47] which pose a new addition to the emerging family of solid-state thermomaterials for eco-friendly heating and/or cooling applications. In addition, the obtained results highlight the interest of small chemical modification (*i.e.* halide substitution) to modulate and enhance the barocaloric properties in hybrid ionic crystals.

3.5. Dielectric properties

Relative permittivity *versus* temperature measurements allowed us to better understand the mechanism of the phase transition observed in these compounds and also to study the materials dielectric response to an external electric field.

Fig. 10 shows the temperature dependence of the real part of the complex dielectric permittivity (ε'_r). The data shows that these compounds exhibit increase in the real part of the dielectric permittivity at the phase transition. This can be attributed to changes in the molecular dynamics of the polar $[(CH_3CH_2)_3N(CH_2X)]^+$ cations at the transition. In the LT-phase, the cations are ordered or in static disorder, meaning that their dipoles maintain a fixed orientation. As the temperature increases beyond the phase transition, the cations shift to a dynamically disordered state where their dipoles reoriented rapidly. The transition to the HT phase with enhanced mole-

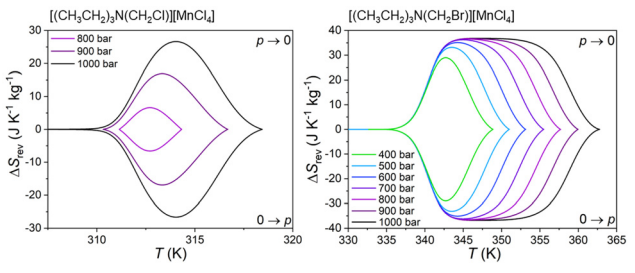

Fig. 8 Reversible isothermal entropy changes on applying (0 → *p*) and removing (*p* → 0) pressure obtained by quasidirect methods of $[(CH_3CH_2)_3N(CH_2Cl)]_2[MnCl_4]$ (left) and $[(CH_3CH_2)_3N(CH_2Br)]_2[MnCl_4]$ (right).

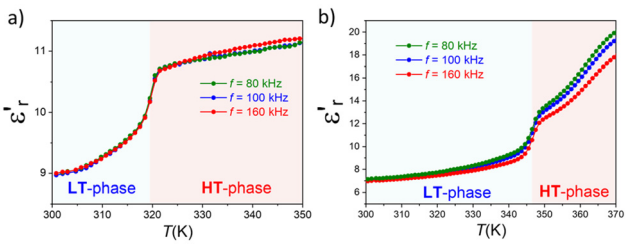

Fig. 10 Temperature-dependence of the dielectric permittivity of $[(CH_3CH_2)_3N(CH_2X)]_2[MnCl_4]$ where (a) X = Cl and (b) X = Br during the heating and cooling runs, at 80, 100 and 160 kHz.

cular rotation typically involves an expansion of the unit cell and weakening of the intermolecular bonding which can allow greater molecular displacement in response to the electric field.

3.6. Photoluminescence properties

When stimulated with ultraviolet (UV) radiation, both compounds emit green light. Notably, the emission from the Br-compound is more intense than that of the Cl-compound, a difference that is clearly observable even to the naked eye (see Fig. 11).

Fig. 12 show the photoluminescence (PL) emission and PL excitation (PLE) spectra at room temperature. The PL spectra are characterized by a single peak centred around 518 nm, with a narrow full width at half maximum (FWHM) of approximately 60 nm in both compounds. This green emission is originated by the $^4T_1 \rightarrow {}^6A_1$ transition.

The PLE spectra exhibit two distinct groups of bands in the region between 300 and 500 nm, which correspond to $^6A_1 \rightarrow {}^4G$ (around 420–500 nm) and $^6A_1 \rightarrow {}^4D$ (around 350–390 nm) transitions.[22,48]

Additionally, we investigated the temperature-dependent photoluminescence (PL) emission over the range of 293–373 K (see Fig. 13) to assess how the phase transition affects the PL properties of these compounds. In general, the PL emission intensity decreases with increasing temperature, and the emission of the Br-compound is completely quenched in its HT phase.

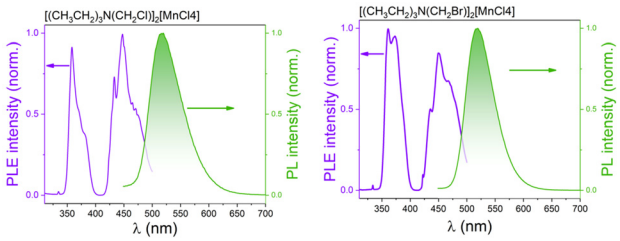

Fig. 11 Images of $[(CH_3CH_2)_3N(CH_2Cl)]_2[MnCl_4]$ and $[(CH_3CH_2)_3N(CH_2Br)]_2[MnCl_4]$ compounds under visible light (left) and UV light by a handheld UV lamp of λ = 365 nm (right).

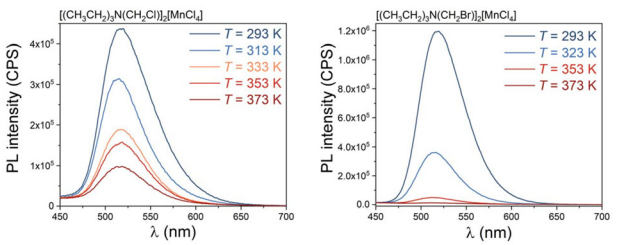

Fig. 12 The PLE and PL spectra of $[(CH_3CH_2)_3N(CH_2Cl)]_2[MnCl_4]$ and $[(CH_3CH_2)_3N(CH_2Br)]_2[MnCl_4]$ compounds measured at room temperature. The PL spectra was excited with wavelength of λ = 360 nm and PLE spectra was registered at the wavelength of λ = 518 nm.

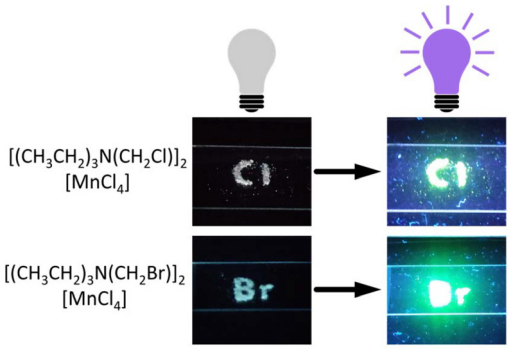

Fig. 13 Temperature-dependent PL spectra of $[(CH_3CH_2)_3N(CH_2Cl)]_2[MnCl_4]$ and $[(CH_3CH_2)_3N(CH_2Br)]_2[MnCl_4]$ compounds. The PL spectra was excited with wavelength of λ = 360 nm.

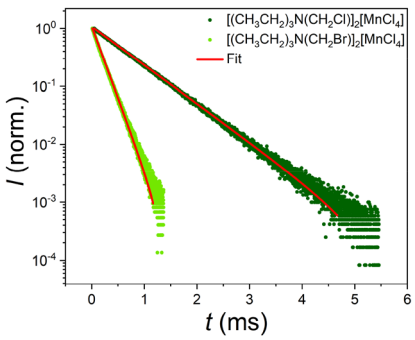

Fig. 14 Emission decay curves for $[(CH_3CH_2)_3N(CH_2Cl)]_2[MnCl_4]$ and $[(CH_3CH_2)_3N(CH_2Br)]_2[MnCl_4]$ compounds at room temperature.

Fig. 14 shows the decay time of the PL emission at room temperature. These curves were fitted to a single-order exponential decay function to estimate the average lifetime, yielding τ = 175 μs for Br-compound and τ = 650 μs for Cl-compound. These relatively large values of emission decay are related to the forbidden nature of the $^4T_1 \rightarrow {}^6A_1$ transition, which slows the emission. Notably, the Cl-compound's decay time is nearly three times longer than that of the Br-compound. Moreover, the average lifetimes obtained here are consistent with those reported for analogous 0D $[MnCl_4]^{2-}$ compounds, which range between 200 and 4000 μs.[49]

Finally, we estimated the photoluminescence quantum yield (PLQY) of both compounds, finding very different values for the Cl-compound (approximately 12%) and the Br-compound (43%). It is worth to note that the Br-compound with the shorter PL lifetime has the higher photoluminescence yield.

In this context, it is known that PLQY increases exponentially with the Mn–Mn distances between neighbouring $[MnCl_4]^{2-}$ tetrahedra.[50] It is worth to note that the sizes of the $[(CH_3CH_2)_3N(CH_2Cl)]^+$ and $[(CH_3CH_2)_3N(CH_2Br)]^+$ cations are slightly different due to the larger size of the Br atom compared to the Cl atom, which results in a larger Mn–Mn distance in the Br compound. Additionally, H-bonds can also

increase or decrease the non-radiative relaxation probability of the excited states of the cations and $[MnX_4]^{2-}$ anions, influencing the luminescence lifetimes and quantum yields.[51,52] In these compounds, the intermolecular interactions between the organic cations and $[MnCl_4]^{2-}$, as well as the intramolecular Mn–Cl bond lengths, are influenced by the nature of the halide atom. The intermolecular interactions between the organic cations and $[MnCl_4]^{2-}$, as well as the intramolecular Mn–Cl bond lengths, are influenced by the nature of the halide atom. The higher electronegativity of Cl favours intermolecular interactions (H-bonds) and shortens the Mn–Mn distance in the Cl-compound. Also, this intermolecular bonding influences the intramolecular Mn–Cl bonds. Morad *et al.* reported that weaker fields and less covalent Mn–X bonds result in less efficient emission.[25] We suggest that this effect occurs in these compounds. As previously described, the organic cation containing a chloride atom, which is highly electronegative, causes stronger intermolecular interactions with $[MnCl_4]^{2-}$ tetrahedra and induces a weakening of the Mn–Cl bond. In contrast, the lower electronegativity of the bromide atoms results in weaker intermolecular interactions and stronger Mn–Cl bonds. Therefore, these differences explain the variations in the photoluminescence (PL) response of both compounds.

4. Conclusions

We have synthesized, structurally characterized, and compared the functional properties of two tetrachloromanganate(II) compounds, one of them novel, with formula $[(CH_3CH_2)_3N(CH_2X)]_2[MnCl_4]$ (with X = Cl, Br). Our results demonstrate that these compounds are highly versatile, exhibiting broad functional responses to external stimuli. Moreover, the obtained results demonstrate that their multi-responsive behaviour can be tuned through subtle modifications in chemical composition; for instance, replacing the halogen in the ammonium cations from Cl to Br induces significant changes in their properties.

Both compounds exhibit a solid–solid phase transition, occurring at approximately 318 K for the Cl-compound and 343 K for the Br-compound. For $[(CH_3CH_2)_3N(CH_2Cl)]_2[MnCl_4]$, we determined the crystal structures in both the LT and HT phases. Our structural analysis reveals that the phase transition is primarily driven by changes in the behavior of the $[(CH_3CH_2)_3N(CH_2Cl)]^+$ cations, while the $[MnCl_4]^{2-}$ anions remain fully ordered in both phases. In the LT phase, the cations are either completely ordered, positionally disordered or orientationally disordered. In contrast, upon transitioning to the HT phase, all the cations exhibit dynamic orientational disorder, rapidly reorienting themselves in response to the increased thermal energy —a pronounced shift that is key to understanding the associated dielectric anomaly—.

Furthermore, substituting the cation halide from Cl to Br increases the phase transition temperature by approximately 25 K and significantly enhances the photoluminescent properties, with the Br-compound showing a photoluminescence quantum yield about four times higher than that of the Cl-compound. Additionally, our investigation of the pressure dependence and barocaloric properties revealed relatively high dT/dp values, comparable to those of other hybrid materials, and demonstrated reversible barocaloric effects under pressures below 1000 bar. Notably, the Br-compound exhibits full reversible BC response at pressures as low as 600 bar.

These results highlight the high tunability and potential of this family of compounds for advanced multifunctional materials and their applications.

Author contributions

J. G.-B. was involved in most of the experimental work. S. C.-G., M. A. S.-R., J. M. B.-G. and M. S.-A. conceived the project. M. G., P. D.-R., A. F.-M., A. G.-F. and U. B. C. were involved in photoluminescence measurements. I. D.-F. was involved in barocaloric measurements. J. L.-B. and R. A. were involved in room temperature VT-DSC measurements. M. S.-A., J. M. B.-G., J. W. and C. J. M. were involved in VT-SPXRD experiments. S. C.-G. and M. S.-A. were involved in SC-XRD experiments. All authors were involved in the discussion of results and in the manuscript writing and revision. M. S.-A. and J. M. B.-G. directed and supervised this project.

Conflicts of interest

There are no conflicts to declare.

Data availability

The data supporting this article have been included as part of the ESI.†

The crystallographic data can be found in Cambridge Crystallographic Data Centre (CCDC) *via* **https://www.ccdc.cam.ac.uk/services/structure_deposit** with CCDC numbers: 2427806–2427812.†

For additional information, please contact the corresponding authors.

Acknowledgements

The authors thank financial support from grant PID2021-122532OB-I00 funded by MCIN/AEI/10.13039/501100011033 and ERDF A way of making Europe, the project PDC2021-121076-I00 funded by MCIN/AEI/10.13039/501100011033 and by the European Union Next GenerationEU/PRTR, and the projects ED431C 2022/39 and ED431F 2023/33 funded by Xunta de Galicia. This publication is part of the grant RYC2021-033040-I, funded by MCIN/AEI/10.13039/501100011033 and from European Union "NextGenerationEU"/PRTR", and granted to J. M. B.-G. This researcher is also grateful for the

support received by UDC-Inditex InTalent Programme. J. G.-B. and M. G. acknowledge Xunta de Galicia for Postdoctoral (ED481B-2024) and Predoctoral (ED481A-2023) Fellowships, respectively. P. D.-R. thanks Ministerio de Ciencia, Innovación y Universidades for a FPU Fellowship (FPU23/00091). A. G.-F. and U. B. C. thank the Swedish Research Council (Grant No. VR 2022-03168) and the Göran Gustafsson foundation for funding. This work was partially supported by the Wallenberg Initiative Materials Science for Sustainability (WISE) funded by the Knut and Alice Wallenberg Foundation. A. G.-F acknowledges support from a Beatriz Galindo junior fellowship (BG23/00033) from the Spanish Ministry of Science and Innovation. The authors thank ESRF for the award of beam time (A01-2-1291 on BM01). Open access publication fees were covered by Universidade da Coruña/CISUG.

References

1 F. X. Coudert, Responsive metal-organic frameworks and framework materials: Under pressure, taking the heat, in the spotlight, with friends, *Chem. Mater.*, 2015, **27**, 1905–1916.

2 Y. Ge, P. Lv, C. A. Schalley and Z. Qi, Chapter 3: Multi-stimuli Responsive Materials, in *Chemoresponsive Materials: Smart Materials for Chemical and Biological Stimulation*, ed. H.-J. Schneider, Royal Society of Chemistry, 2022, pp. 47–95.

3 J. Salgado-Beceiro, J. M. Bermúdez-García, A. L. Llamas-Saiz, S. Castro-García, M. A. Señarís-Rodríguez, F. Rivadulla and M. Sánchez-Andújar, Multifunctional properties and multi-energy storage in the [(CH$_3$)3S][FeCl4] plastic crystal, *J. Mater. Chem. C*, 2020, **8**, 13686–13694.

4 J. García-Ben, J. López-Beceiro, R. Artiaga, J. Salgado-Beceiro, I. Delgado-Ferreiro, Y. V. Kolen'ko, S. Castro-García, M. A. Señarís-Rodríguez, M. Sánchez-Andújar and J. M. Bermúdez-García, Discovery of Colossal Breathing-Caloric Effect under Low Applied Pressure in the Hybrid Organic-Inorganic MIL-53(Al) Material, *Chem. Mater.*, 2022, **34**, 3323–3332.

5 M. Gelpi, J. García-Ben, S. Rodríguez-Hermida, J. López-Beceiro, R. Artiaga, Á. Baaliña, M. Romero-Gómez, J. Romero-Gómez, S. Zaragoza, J. Salgado-Beceiro, J. Walker, C. J. McMonagle, S. Castro-García, M. Sánchez-Andújar, M. A. Señarís-Rodíguez and J. M. Bermúdez-García, Empowering CO2 Eco–Refrigeration with Colossal Breathing–Caloric–Like Effects in MOF-508b, *Adv. Mater.*, 2024, **36**, 2310499.

6 D. D. Yang, F. Q. Meng, H. W. Zheng, Y. S. Shi, T. Xiao, B. Jin, Q. F. Liang, X. J. Zheng and H. W. Tan, Two multifunctional stimuli-responsive materials with room-temperature phosphorescence and their application in multiple dynamic encryption, *Mater. Chem. Front.*, 2022, **6**, 2709–2717.

7 A. Cuquejo-Cid, A. García-Fernández, J. García-Ben, M. A. Señarís-Rodríguez, S. Castro-García, M. Sánchez-Andújar and D. Vázquez-García, Photoluminescent and vapochromic properties of the Mn(II)-doped (C6H11NH3)2PbBr4 layered organic–inorganic hybrid perovskite, *Polyhedron*, 2021, **193**, 114840.

8 H. Son and C. Yoon, Advances in stimuli-responsive soft robots with integrated hybrid materials, *Actuators*, 2020, **9**, 1–19.

9 J. Walker, K. P. Marshall, J. Salgado-Beceiro, B. A. D. Williamson, N. S. Løndal, S. Castro-Garcia, M. S. Andújar, S. M. Selbach, D. Chernyshov and M. A. Einarsrud, Mesophase Transitions in [(C2H5)4N][FeBrCl3] and [(CH$_3$)4N][FeBrCl3] Ferroic Plastic Crystals, *Chem. Mater.*, 2022, **34**, 2585–2598.

10 D. Li, X. Sun, S. Jiao, W. Zhang, Y. Lu, M. Zhao, Y. Wu, H. L. Cai and X. Wu, A novel zero-dimensional organic-inorganic hybrid ferroelectric material, *J. Mater. Chem. C*, 2024, **12**, 4267–4272.

11 J. Salgado-Beceiro, J. M. Bermúdez-García, E. Stern-Taulats, J. García-Ben, S. Castro-García, M. Sánchez-Andújar, X. Moya and M. A. Señarís-Rodríguez, Hybrid ionic plastic crystals in the race for enhanced low-pressure barocaloric materials, *ChemRxiv*, 2021, 17–19.

12 B. M. P. Beebeejaun-Boodoo, R. Erasmus and M. Rademeyer, Tetrahalometallate salts of: N -(4-picolinium)-1,8-naphthalimide: Structures and solid-state fluorescence, *CrystEngComm*, 2018, **20**, 4875–4887.

13 C. Belloso-Casuso, I. de Pedro, L. Canadillas-Delgado, G. Beobide, M. Sánchez-Andújar, J. García-Ben, J. Walker, P. González Izquierdo, I. Cano, J. Rodríguez Fernández and O. Fabelo, Structural and Physico-Chemical Characterization of Hybrid Materials Based on Globular Quinuclidinum Cations Derivatives and Tetrachloridocobaltate(II) Anions, *CrystEngComm*, 2024, **26**, 439–451.

14 A. Salvatori, D. Aguilà, G. Aromí, L. Mañosa, A. Planes, P. Lloveras, L. C. Pardo, M. Appel, G. F. Nataf, F. Giovannelli, M. Barrio, J. L. Tamarit and M. Romanini, Large barocaloric effects in two novel ferroelectric molecular plastic crystals, *J. Mater. Chem. A*, 2023, **11**, 12140–12150.

15 D. Li, X. M. Zhao, H. X. Zhao, L. S. Long and L. S. Zheng, Coexistence of Magnetic-Optic-Electric Triple Switching and Thermal Energy Storage in a Multifunctional Plastic Crystal of Trimethylchloromethyl Ammonium Tetrachloroferrate(III), *Inorg. Chem.*, 2019, **58**, 655–662.

16 J. Salgado-Beceiro, S. Castro-García, M. Sánchez-Andújar and F. Rivadulla, Motional Narrowing of Electron Spin Resonance Absorption in the Plastic-Crystal Phase of [(CH$_3$)4N]FeCl4, *J. Phys. Chem. C*, 2018, **122**, 27769–27774.

17 B. Wang, J. Hong, Y. Yang, H. Zhao, L. Long and L. Zheng, Achievement of a giant piezoelectric coefficient and piezoelectric voltage coefficient through plastic molecular-based ferroelectric materials, *Matter*, 2022, **5**, 1296–1304.

18 W. Wang, C. D. Liu, X. B. Han, C. Q. Jing, C. Y. Chai, C. C. Fan, M. L. Jin, J. M. Zhang and W. Zhang, Photoluminescence Switching and Non-Volatile Memory in

Hybrid Metal-Halide Phase-Change Materials, *ACS Mater. Lett.*, 2024, **6**, 203–211.

19 Z. Wang and X. Huang, Luminescent Organic-Inorganic Hybrid Metal Halides: An Emerging Class of Stimuli-Responsive Materials, *Chem. – Eur. J.*, 2022, **28**, e202200609.

20 Y. M. Liu, K. Li, T. M. Guo, L. C. An, Z. Z. Zhang, M. H. Yu, W. Li and X. H. Bu, Ammonium Sulfate Structure-Type Hybrid Metal Halide Ferroelectric with Giant Uniaxial Spontaneous Strain, *ACS Mater. Lett.*, 2022, **4**, 1168–1173.

21 H. Fu, C. Jiang, C. Luo, H. Lin and H. Peng, Manganese halide hybrids with a reversible luminous color and their application for a white light-emitting diode, *CrystEngComm*, 2022, **24**, 6910–6916.

22 L. Mao, P. Guo, S. Wang, A. K. Cheetham and R. Seshadri, Design Principles for Enhancing Photoluminescence Quantum Yield in Hybrid Manganese Bromides, *J. Am. Chem. Soc.*, 2020, **142**, 13582–13589.

23 A. S. Berezin, M. P. Davydova, D. G. Samsonenko, T. S. Sukhikh and A. V. Artem'ev, A family of brightly emissive homo- and mixed-halomanganates(II): The effect of halide on optical and magnetic properties, *J. Lumin.*, 2021, **236**, 118069.

24 K. Xu and A. Meijerink, Tuning Exciton-Mn2+ Energy Transfer in Mixed Halide Perovskite Nanocrystals, *Chem. Mater.*, 2018, **30**, 5346–5352.

25 V. Morad, I. Cherniukh, L. Pöttschacher, Y. Shynkarenko, S. Yakunin and M. V. Kovalenko, Manganese(II) in Tetrahedral Halide Environment: Factors Governing Bright Green Luminescence, *Chem. Mater.*, 2019, **31**, 10161–10169.

26 J. Garcia-Ben, J. M. Bermúdez-García, R. J. C. Dixey, I. Delgado-Ferreiro, A. L. Llamas-Saiz, J. López-Beceiro, R. Artiaga, A. Garcia-Fernandez, U. B. Cappel, B. Alonso, S. Castro-Garcia, A. E. Phillips, M. Sánchez-Andújar and M. A. Señarís-Rodríguez, Structure and thermal properties relationships in the thermomaterial di-n-butylammonium tetrafluoroborate for multipurpose cooling and cold-storage, *J. Mater. Chem. A*, 2023, **11**, 22232–22247.

27 J. García-Ben, I. Delgado-Ferreiro, R. J. C. Dixey, S. Castro-García, J. López-Beceiro, R. Artiaga, M. Sánchez-Andújar, A. E. Phillips, J. M. Bermúdez-García and M. A. Señarís-Rodríguez, Unveiling barocaloric potential in organo-metallic-sandwich compounds [Cp2M][PF6] (M: Fe3+, Co3+), *J. Mater. Chem. A*, 2024, **12**, 23751–23760.

28 P. Dafonte-Rodriguez, I. Delgado-Ferreiro, J. Garcia-Ben, A. Ferradanes-Martinez, M. Gelpi, J. Walker, C. J. McMonagle, S. Castro-Garcia, M. A. Senaris-Rodriguez, J. M. Bermudez-Garcia and M. Sánchez-Andujar, Exploring the effect of pressure on the crystal structure and caloric properties of the molecular ionic hybrid [(CH_3)3NOH]2 [CoCl4], *Chem. Commun.*, 2024, **60**, 14065–14068.

29 C. C. Sun, W. Li, D. X. Liu, Z. Y. Du, C. T. He, W. X. Zhang and X. M. Chen, Insights into the Molecular Dynamics of Quasi-Spherical (Chloromethyl)triethylammonium Confined in a Weakly Bound Ionic Cocrystal, *Inorg. Chem.*, 2022, **61**, 7201–7206.

30 Y. Zhang, Z. Cai, X. Zhang, S. Xiao, X. Liu, Y. Zhao, X. N. Hua and B. Sun, Dielectric and optical properties of a new organic–inorganic hybrid phase transition material, *CrystEngComm*, 2023, **25**, 4284–4289.

31 J. García-Ben, A. García-Fernández, P. Dafonte-Rodríguez, I. Delgado-Ferreiro, U. B. Cappel, S. Castro-García, M. Sánchez-Andújar, J. M. Bermúdez-García and M. A. Señarís-Rodríguez, Narrowing the tolerance factor limits for hybrid organic-inorganic dicyanamide-perovskites, *J. Solid State Chem.*, 2022, **316**, 123635.

32 G. M. Sheldrick, SHELXT - Integrated space-group and crystal-structure determination, *Acta Crystallogr., Sect. A: Found. Crystallogr.*, 2015, **71**, 3–8.

33 J. Kieffer, J. Orlans, N. Coquelle, S. Debionne, S. Basu, A. Homs, G. Santoni and D. De Sanctis, Application of signal separation to diffraction image compression and serial crystallography, *J. Appl. Crystallogr.*, 2025, **58**, 138–153.

34 V. Dyadkin, P. Pattison, V. Dmitriev and D. Chernyshov, A new multipurpose diffractometer PILATUS@SNBL, *J. Synchrotron Radiat.*, 2016, **23**, 825–829.

35 B. H. Toby and R. B. Von Dreele, GSAS-II: The genesis of a modern open-source all purpose crystallography software package, *J. Appl. Crystallogr.*, 2013, **46**, 544–549.

36 M. J. Cliffe and A. L. Goodwin, PASCal: A principal axis strain calculator for thermal expansion and compressibility determination, *J. Appl. Crystallogr.*, 2012, **45**, 1321–1329.

37 P. R. Spackman, M. J. Turner, J. J. McKinnon, S. K. Wolff, D. J. Grimwood, D. Jayatilaka and M. A. Spackman, CrystalExplorer: A program for Hirshfeld surface analysis, visualization and quantitative analysis of molecular crystals, *J. Appl. Crystallogr.*, 2021, **54**, 1006–1011.

38 J. J. B. Levinsky, S. Grover, P. Partridge, E. Dempsey, C. J. Mcmonagle and C. L. Hobday, The role of hydrogen bond competition in the colossal barocaloric response of choline-based hybrid ionic plastic crystals [choline] 2 CoCl 4 and, *ChemRxiv*, 2024, 1–22.

39 N. A. Wojcik, D. A. Kowalska, M. Trzebiatowska, E. Jach, A. Ostrowski, W. Bednarski, M. Gusowski, P. Staniorowski and A. Cizman, Tunable Dielectric Switching of (Quinuclidinium)[MnCl4] Hybrid Compounds, *J. Phys. Chem. C*, 2021, **125**, 16810–16818.

40 X. Moya, S. Kar-Narayan and N. D. Mathur, Caloric materials near ferroic phase transitions, *Nat. Mater.*, 2014, **13**, 439–450.

41 J. M. Bermúdez-García, M. Sánchez-Andújar, S. Castro-García, J. López-Beceiro, R. Artiaga and M. A. Señarís-Rodríguez, Giant barocaloric effect in the ferroic organic-inorganic hybrid [TPrA][Mn(dca)3] perovskite under easily accessible pressures, *Nat. Commun.*, 2017, **8**, 15715.

42 J. Seo, R. D. McGillicuddy, A. H. Slavney, S. Zhang, R. Ukani, A. A. Yakovenko, S. L. Zheng and J. A. Mason, Colossal barocaloric effects with ultralow hysteresis in two-dimensional metal–halide perovskites, *Nat. Commun.*, 2022, **13**, 1–15.

43 C. Escorihuela-Sayalero, L. C. Pardo, M. Romanini, N. Obrecht, S. Loehlé, P. Lloveras, J.-L. Tamarit and C. Cazorla, Prediction and understanding of barocaloric effects in orientationally disordered materials from molecular dynamics simulations, *npj Comput. Mater.*, 2024, **10**, 13.

44 J. M. Bermúdez-García, S. Yáñez-Vilar, A. García-Fernández, M. Sánchez-Andújar, S. Castro-García, J. López-Beceiro, R. Artiaga, M. Dilshad, X. Moya and M. A. Señarís-Rodríguez, Giant barocaloric tunability in [(CH_3CH2CH2)4N]Cd[N(CN)2]3 hybrid perovskite, *J. Mater. Chem. C*, 2018, **6**, 9867–9874.

45 J. Li, M. Barrio, D. J. Dunstan, R. Dixey, X. Lou, J. L. Tamarit, A. E. Phillips and P. Lloveras, Colossal Reversible Barocaloric Effects in Layered Hybrid Perovskite (C10H21NH3)2MnCl4 under Low Pressure Near Room Temperature, *Adv. Funct. Mater.*, 2021, **31**, 2105154.

46 J. Salgado-Beceiro, A. Nonato, R. X. Silva, A. García-Fernández, M. Sánchez-Andújar, S. Castro-García, E. Stern-Taulats, M. A. Señarís-Rodríguez, X. Moya and J. M. Bermúdez-García, Near-room-temperature reversible giant barocaloric effects in [(CH_3)4N]Mn[N3]3 hybrid perovskite, *Mater. Adv.*, 2020, **1**, 3167–3170.

47 Y. Gao, H. Liu, F. Hu, H. Song, H. Zhang, J. Hao, X. Liu, Z. Yu, F. Shen, Y. Wang, H. Zhou, B. Wang, Z. Tian, Y. Lin, C. Zhang, Z. Yin, J. Wang, Y. Chen, Y. Li, Y. Song, Y. Shi, T. Zhao, J. Sun, Q. Huang and B. Shen, Reversible colossal barocaloric effect dominated by disordering of organic chains in (CH_3–(CH2)n–1–NH3)2MnCl4 single crystals, *NPG Asia Mater.*, 2022, **14**, 34.

48 Y. L. Wei, J. Jing, C. Shi, H. Y. Ye, Z. X. Wang and Y. Zhang, High quantum yield and unusual photoluminescence behaviour in tetrahedral manganese(II) based on hybrid compounds, *Inorg. Chem. Front.*, 2018, **5**, 2615–2619.

49 C. Luo, J. Li, R. Zhang, P. Han, J. Liu and B. Yang, Quantitative Decoupling of Strong Mn–Mn Coupling on Photoluminescence of Zero-Dimensional Hybrid Manganese Chlorides Single Crystals, *Adv. Opt. Mater.*, 2024, **12**, 2401591.

50 H. M. Pan, Q. L. Yang, X. X. Xing, J. P. Li, F. L. Meng, X. Zhang, P. C. Xiao, C. Y. Yue and X. W. Lei, Enhancement of the photoluminescence efficiency of hybrid manganese halides through rational structural design, *Chem. Commun.*, 2021, **57**, 6907–6910.

51 A. S. Berezin, A halomanganates(II) with P,P′-diprotonated bis(2-diphenylphosphinophenyl)ether: Wavelength-excitation dependence of the quantum yield and role of the non-covalent interactions, *Int. J. Mol. Sci.*, 2021, **22**, 6873.

52 L. K. Gong, Q. Q. Hu, F. Q. Huang, Z. Z. Zhang, N. N. Shen, B. Hu, Y. Song, Z. P. Wang, K. Z. Du and X. Y. Huang, Efficient modulation of photoluminescence by hydrogen bonding interactions between inorganic [MnBr4]2- anions and organic cations, *Chem. Commun.*, 2019, **55**, 7303–7306.

